Research Article | Open Access

Complex Engineering Systems

Zhang et al. Complex Eng. Syst. 2026, 6, 3 DOI: 10.20517/ces.2025.82

A spatial multi-scale reservoir computing framework for power flow analysis in power grids

Hai-Feng Zhang[1], Yu-Miao Zhang[2], Xiao Ding[1], Chuang Ma[3], Yongxiang Xia[4], Chi K. Tse[5]

Keywords:
Power flow, reservoir computing, physical information, functional matrix, spatial multi-scale

Citation: Zhang, H. F.; Zhang, Y. M.; Ding, X.; Ma, C.; Xia, Y.; Tse, C. K. A spatial multi-scale reservoir computing framework for power flow analysis in power grids. *Complex Eng. Syst.* **2026**, *6*, 3. http://dx.doi.org/10.20517/ces.2025.82

Received: 27 Nov 2025 **First Decision:** 31 Dec 2025 **Revised:** 13 Jan 2026 **Accepted:** 26 Jan 2026 **Published:** 12 Feb 2026

Academic Editors: Duxin Chen, Wenwu Yu
Copy Editor: Fangling Lan
Production Editor: Fangling Lan

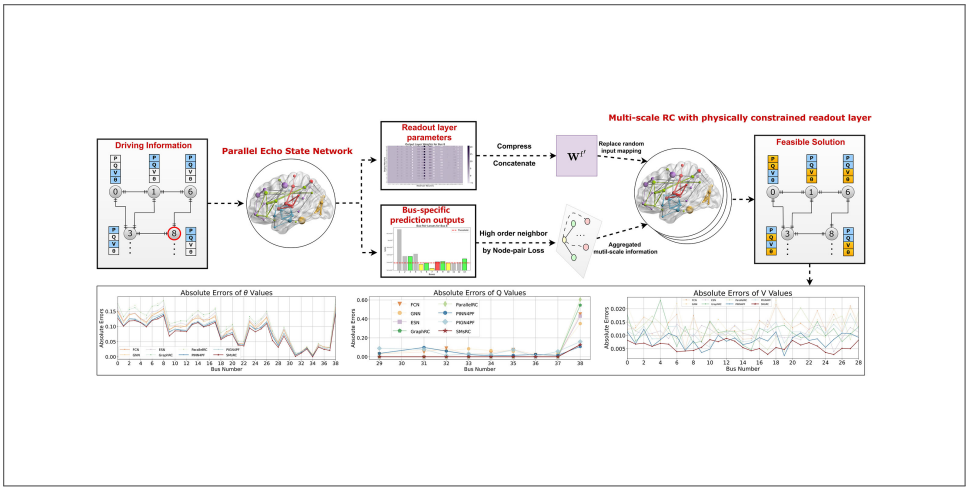

Abstract

With the ongoing evolution of modern power grids, power flow calculation, which is the cornerstone of power system analysis and operation, has become increasingly complex. While promising, existing data-driven methods struggle with key challenges: poor generalization in data-scarce scenarios, efficiency bottlenecks when integrating physical laws, and a failure to capture higher-order interactions within the grid. To address these challenges, this paper proposes a Spatial Multi-scale Reservoir Computing framework that seamlessly incorporates functional matrix and physical information to solve power flow calculation. The framework utilizes parallel readout layer parameters to construct the functional matrix and integrates physical information to create a multi-scale information processing mechanism and readout constraints. By improving the reservoir computing model, the framework also combines the reservoir paradigm with the inherent physical characteristics of power grids

[1]The Key Laboratory of Intelligent Computing and Signal Processing of Ministry of Education, School of Mathematical Science, Anhui University, Hefei 230601, Anhui, China.
[2]The Key Laboratory of Intelligent Computing and Signal Processing of Ministry of Education, Institutes of Physical Science and Information Technology, Anhui University, Hefei 230601, Anhui, China.
[3]School of Internet, Anhui University, Hefei 230601, Anhui, China.
[4]School of Communication Engineering, Hangzhou Dianzi University, Hangzhou 310018, Zhejiang, China.
[5]Department of Electrical Engineering, City University of Hong Kong, Kowloon 999077, China.

Correspondence to: Prof. Yongxiang Xia, School of Communication Engineering, Hangzhou Dianzi University, Hangzhou 310018, Zhejiang, China. E-mail: xiayx@hdu.edu.cn; Prof. Chi K. Tse, Department of Electrical Engineering, City University of Hong Kong, Kowloon 999077, China. E-mail: michael.tse@cityu.edu.hk

while maintaining computational efficiency. Experimental results demonstrate that the presented framework achieves exceptional performance across various IEEE bus systems, showcasing superior generalization in data-scarce scenarios, as well as improvement in computational speed, prediction accuracy, and robustness, while ensuring the feasibility of the output results.

1. INTRODUCTION

With the evolution of the economy and the profound changes in the energy generation and consumption, the scale and structure of modern power grids have become increasingly diverse, and the operational characteristics of the system have become more complex, while also facing greater uncertainties[1,2]. Power flow calculation, as a fundamental component of power system analysis and operation, is also a prerequisite for advanced applications such as stability analysis and optimal dispatching, playing a critical role in ensuring the safe and economical operation of power grids[3,4]. However, in the face of highly nonlinear modern power grids, some traditional numerical methods or heuristic methods often have problems such as non-convergence or low computational efficiency when solving power flow, which make them face considerable challenges in computation and decision support[5,6].

To address these challenges, researchers have increasingly focused on the application of artificial intelligence, especially machine learning and deep learning, in power system analysis and power flow calculations[7,8,9]. These methods have shown significant potential to improve computational speed and handle complex nonlinear relationships. Some of the early data-driven models faced challenges such as limited generalization, inadequate consideration of underlying physical mechanisms, and insufficient accounting for the local-global topological interdependence they entail, especially when applied to highly nonlinear and dynamically evolving complex systems such as power grids[10,11]. Later, with the rise of the graph neural and physics-informed approaches, researchers have sought to integrate the physical mechanisms or topology of power grids with data-driven models[12], but these also introduce the challenge of balancing model complexity and computational efficiency. Moreover, due to the complex and special nature of the electrical environment, models sometimes also face challenges in robustness and data scarcity[13].

Recently, a computational framework known as reservoir computing (RC) has attracted significant attention in the study of complex systems[14,15]. This paradigm circumvents the need for backpropagating error signals, thereby enhancing both robustness and training efficiency. Owing to the high-dimensional and nonlinear dynamics of the reservoir, RC can effectively extract rich and distinguishable dynamic features from the system, even with limited historical data[16]. The RC paradigm has seen some exploratory applications in power systems[17], which are typical complex dynamical systems, but RC's use for analyzing power flow remains quite limited.

Motivated by these challenges, this paper proposes the Spatial Multi-scale Reservoir Computing (SMsRC) framework to improve standard RC for power flow calculation. It has three key innovations: first, a functional matrix is introduced to deterministically encode each bus's role, overcoming the limitations of random input weights; second, a spatial multi-scale analysis captures complex dependencies from higher-order, non-local neighbors; third, physical information is incorporated as a constraint on the readout layer to ensure outputs obey fundamental power flow laws. The main contributions are summarized as follows:

- Considering the advantages of the RC in efficiency and stability, especially for limited-data scenarios, a novel spatial multi-scale reservoir model is proposed and integrated with physical mechanisms to construct a power flow solving framework named SMsRC.

- Three core innovations are introduced in the SMsRC framework. First, a functional matrix replaces random input weights to encode each bus's role, providing data-driven priors. Second, a multi-scale spatial structure captures complex dependencies from higher-order and non-local neighbors for a fuller system representation. Third, physical constraints are applied directly to the RC readout layer, ensuring outputs follow basic power flow laws while maintaining efficiency.

- The performance of the SMsRC framework is validated in solving the power flow across different IEEE bus systems. Compared with other data-driven methods, particularly in the few-shot scenario, the SMsRC demonstrates stronger generalizability, achieving faster training and prediction while ensuring accuracy. Meanwhile, SMsRC shows robustness for diverse power grid scenarios.

The remainder of this article is organized as follows. Section 2 reviews the related work. Section 3 introduces the preliminary concepts and problem definitions. Section 4 outlines the proposed SMsRC framework in detail. Section 5 presents the experimental setup along with the results, and finally, Section 6 concludes the paper with discussions.

2. RELATED WORK

Current methods for power flow calculation fall into three categories: traditional numerical methods, heuristic search methods, and data-driven methods.

2.1. Traditional numerical methods

Numerical methods model power grid operational constraints and objective functions as mathematical equations, deriving optimal flow solutions via numerical iterations[18]. Examples include the Newton-Raphson, Gauss-Seidel, and fast-decoupled power flow methods, *etc.*[19]. Additionally, to improve the convergence, Niu *et al.*[20] designed methods based on Taylor series expansion and improved Newton methods. Montoya *et al.*[21] proposed backward/forward sweep methods based on graph theory and improved algorithms based on rectangular coordinates, improving calculation speed and accuracy under specific conditions. Tang *et al.*[22] developed an Alternating Current optimal power flow calculation method based on the Quasi-Newton method. Despite these advancements, fundamentally, the non-linear and non-convex nature of the alternating current optimal power flow (AC-OPF) problem means they are computationally intensive, highly sensitive to initial values, and can easily get trapped in local optima, failing to find a global-like solution. This results in a lack of convergence and robustness, rendering them inadequate for the fast-timescale control of modern complex power systems. To address these convergence bottlenecks and sensitivity to initial conditions, heuristic search strategies were introduced to enhance global optimization capabilities.

2.2. Heuristic search methods

Researchers have also explored heuristic search methods for power flow calculation. These methods use novel search mechanisms to enhance exploration and exploitation, improving convergence and accuracy. They are typically used for multi-objective optimization problems difficult for traditional techniques[23,24]. The genetic algorithm was among the first heuristic methods applied to power flow[25]. Others include teaching–learning optimization, metaheuristic algorithms, and differential evolution algorithms[26,27], *etc.*, all of which are used to solve optimal power flow problems involving both continuous and discrete control variables. However, these methods present trade-offs. While often more robust in avoiding poor local optima compared to numerical methods, they are notoriously computationally expensive and time-consuming[28]. Their performance is sensitive to the initial encoding of the problem and the specific design of the fitness function, including the penalty mechanisms for handling operational constraints. And they face persistent challenges in generalizing effectively to high-dimensional nonlinear systems. These computational bottlenecks have motivated the emergence

Table 1. Comparisons of characteristics and limitations among different power flow calculation methods

Category	Representative methods	Characteristics & limitations (pain points)	Evolution & superiority of SMsRC
Traditional numerical methods (Rule-based)	Newton-Raphson, Gauss-Seidel, Fast-decoupled methods (e.g., [18,19,20])	**Char**: Solves mathematical equations based on physical laws via iterations **Limits**: Computationally intensive; highly sensitive to initial values; prone to non-convergence in complex, non-convex AC-OPF problems.	SMsRC replaces the rigid iterative solving process with a learned non-linear mapping, avoiding non-convergence issues while maintaining physical feasibility through constrained readout layers
Heuristic search methods (Evolutionary)	Genetic Algorithm (GA), PSO, Differential Evolution (e.g., [25,26,27])	**Char**: Global optimization mechanisms; effective for discrete variables **Limits**: Extremely computationally expensive and time-consuming; performance is sensitive to encoding and fitness function design	Leveraging the echo state property of Reservoir Computing (RC), SMsRC achieves extremely fast training and inference speeds, addressing the computational bottleneck of heuristic search methods
Existing data-driven methods (Machine learning)	DNN, GNN, PINN (e.g., [32,3,31])	**Char**: Fast inference; automatic feature extraction from data **Limits**: Poor generalization in data-scarce scenarios; often neglects high-order topological dependencies; struggles to strictly guarantee physical consistency (feasibility)	**Addressing data-driven gaps:** 1. **Functional matrix**: Replaces random weights to encode bus roles (Determinis-tic *vs.* Random) 2. **Spatial multi-scale**: Captures long-range/high-order dependencies often missed by standard GNNs 3. **Physical constraints**: Directly integrates power laws into the readout to ensure valid solutions
Proposed framework	**SMsRC** (This paper)	**Char**: A spatial multi-scale reservoir computing framework integrated with functional matrix and physical information	**Synthesis**: SMsRC combines the efficiency of RC with the rigour of physical laws. It demonstrates superior robustness and accuracy, especially in few-shot scenarios where pure data-driven methods fail

of data-driven methods, which aim to learn complex mappings directly from historical data without explicit iterative optimization.

2.3. Data-driven methods

With the rapid advancement of deep learning technologies and the growing complexity of modern power grids, there has been increasing research interest in data-driven approaches. These methods are capable of automatically learning feature patterns directly from data, without the need for precise prior knowledge [29,30]. Currently, the models applied to power flow are primarily based on deep neural networks (DNNs) or graph neural networks (GNNs), as well as physics-informed neural networks expanded on this basis [31]. Hansen *et al.* [32] developed

an end-to-end framework based on line GNNs to balance the power flow in energy grids. Lopez-Garcia*et al.*[3] developed a typed GNN with linear complexity that solves the power flow problem through an unsupervised method of minimizing the violation of physical laws. In addition, ensuring feasible solutions is crucial in power flow problems. Some studies verify or refine model outputs using additional optimizers or classifiers[33], while others enhance accuracy and feasibility by incorporating physical information[34]. However, these approaches often rely on complex penalty-based loss functions to address the limitations of general models such as DNNs or GNNs[35], which can increase computational cost, complicate gradient calculation, and sometimes lead to parameter sensitivity or unstable outputs. These observations motivate our proposed SMsRC framework that can organically integrate physical laws with efficient learning paradigms to simultaneously ensure computational speed and solution feasibility.

To highlight the research gap, Table 1 compares existing methods with the proposed SMsRC framework. SMsRC addresses previous limitations by integrating physical constraints and functional priors, balancing efficiency, generalization, and physical consistency.

3. PRELIMINARIES AND PROBLEM FORMULATION

To rigorously formulate the power flow solving problem addressed in this paper, this section introduces the theoretical and physical foundations alongside the mathematical definition. Specifically, Section 3.1 first outlines the basic principles of RC, which serves as the core computational engine of the proposed framework. Subsequently, Section 3.2 describes the physical characteristics and governing equations of the power flow in power grids, defining the key variables and node types. Finally, based on the computational paradigm introduced in Section 3.1 and the system variables defined in Section 3.2, Section 3.3 formally presents the mathematical formulation of the data-driven power flow calculation problem.

3.1. Reservoir computing (RC)

RC, as a machine learning paradigm that has gained attention in the field of complex systems in recent years, has its core idea in performing nonlinear transformations with the help of a randomly connected neural network (i.e., the reservoir), and then achieving the output of specific tasks by training the weights of the readout layer[36].

Echo State Network (ESN), as a prominent implementation of RC, features a basic architecture comprising three core parts: the input layer, the reservoir, and the readout layer. Operations related to these three parts mainly include initializing the input matrix $\mathbf{W}^{\text{in}} \in \mathbb{R}^{N_x \times N_r}$ and the reservoir adjacency matrix $\mathbf{W} \in \mathbb{R}^{N_r \times N_r}$, updating the reservoir state, and training the readout layer weights $\mathbf{W}^{\text{out}} \in \mathbb{R}^{N_y \times N_r}$. N_x, N_r, and N_y represent the input dimension, the number of reservoir nodes, and the output dimension, respectively. Traditionally, $\mathbf{W}^{\text{in}}$ and $\mathbf{W}$ are fixed after initialization and are typically randomly sampled from a uniform distribution, followed by appropriate sparsification and scaling. In this work, the traditional initialization approach is improved through the construction of a functional matrix, which will be discussed in detail later. A key characteristic of ESN is the "Echo State Property", which ensures that the state of the reservoir is determined primarily by the input rather than by the initial conditions[37]. This is typically achieved by setting the spectral radius ρ of $\mathbf{W}$ to a value close to, but less than 1.

For the problem of the power flow calculation, which is a system of nonlinear equations, the training process of the ESN can be characterized using [38,39]:

$$\mathbf{r}(t+1) = \begin{cases} (1-\alpha)\mathbf{r}(t) + \alpha \cdot \tanh\left(\mathbf{W}^{\text{in}}\,\mathbf{x} + \mathbf{W}\mathbf{r}(t)\right), & t = 1; \\ (1-\alpha)\mathbf{r}(t) + \alpha \cdot \tanh(\mathbf{W}\mathbf{r}(t)), & t > 1, \end{cases} \tag{1}$$

$$\mathbf{y} = \mathbf{W}^{\text{out}}\,\mathbf{r}(T), \tag{2}$$

$$J\left(\mathbf{W}^{\text{out}}\right) = \left\|\mathbf{Y} - \mathbf{R}\mathbf{W}^{\text{out}}\right\|_F^2 + \beta\left\|\mathbf{W}^{\text{out}}\right\|_F^2, \tag{3}$$

$$\mathbf{W}^{\text{out}} = \mathbf{Y}^{\top}\mathbf{R}\left(\mathbf{R}^{\top}\mathbf{R} + \beta\mathbf{I}\right)^{-1}. \tag{4}$$

where $\mathbf{r}(t) \in \mathbb{R}^{N_r}$ is the reservoir state vector, $\mathbf{x} \in \mathbb{R}^{N_x}$ is the input vector, and $\alpha \in (0, 1]$ is the leakage rate. $t_{\max} = T$ is the predefined number of iterations in the reservoir, $\mathbf{W}^{\text{out}}$ is the output weight matrix, and $\mathbf{y} \in \mathbb{R}^{N_y}$ is the output vector. Assuming that there are N training samples, the state matrix $\mathbf{R} = [\mathbf{r}_1(T), \ldots, \mathbf{r}_N(T)]^{\top}$ and the target matrix $\mathbf{Y} = [\mathbf{y}_1, \ldots, \mathbf{y}_N]^{\top}$ can be constructed. $J\left(\mathbf{W}^{\text{out}}\right)$ is the objective function for the ridge regression, where β is the regularization parameter, and $\|\cdot\|_F$ denotes the Frobenius norm.

3.2. Power flow

In power system operations, two primary power flow models are widely used: direct current optimal power flow (DC-OPF) and AC-OPF. Although the DC-OPF model is relatively simple to compute, its precision is compromised due to the variations in reactive power and voltage magnitude. In contrast, the AC-OPF model considers more comprehensive system characteristics, providing a more accurate description of the actual system's operational state. Therefore, this study adopts AC-OPF as the foundational model.

Under steady-state conditions, buses in a power grid can be classified into three types: PQ buses, PV buses, and slack bus. Each type of bus is characterized by distinct known and unknown parameters. Specifically, PQ buses correspond to load nodes, with known active power P and reactive power Q, and unknown voltage magnitude V and stage angle θ; PV buses correspond to generator nodes, with known active power P and voltage magnitude V, and unknown reactive power Q and stage angle θ; slack bus is the sole balance node in the system, with known voltage magnitude V and stage angle θ serving as the global system reference, and unknown active power P and reactive power Q.

The AC-OPF problem seeks to minimize the operational cost of the system while adhering to various physical and operational constraints[40]:

$$\min f\left(P^g, Q^g\right) = \sum_{i=1}^{N_g} f_P^i\left(P_i^g\right) + f_Q^i\left(Q_i^g\right) \tag{5}$$

subject to:

$$P_i^g - P_i^d = \sum_{j \in V}^{N} V_i V_j \left(G_{ij}\cos\theta_{ij} + B_{ij}\sin\theta_{ij}\right), i = 1 \ldots N_b, \tag{6}$$

$$Q_i^g - Q_i^d = \sum_{j \in V}^{N} V_i V_j \left(G_{ij}\sin\theta_{ij} - B_{ij}\cos\theta_{ij}\right), i = 1 \ldots N_b, \tag{7}$$

$$P_i^{g,\min} \le P_i^g \le P_i^{g,\max}, i = 1, \ldots, N_g, \tag{8}$$

$$Q_i^{g,\min} \le Q_i^g \le Q_i^{g,\max}, i = 1, \ldots, N_g, \tag{9}$$

$$V_i^{\min} \le V_i \le V_i^{\max}, i = 1, \ldots, N_b, \tag{10}$$

$$\left|\theta_{ij}\right| \le \theta_{ij}^{\max}, (i, j) \in \mathcal{E}. \tag{11}$$

where N_b and N_g represent the numbers of buses and generators in the system, respectively. The functions $f_P^i\left(P_i^g\right)$ and $f_Q^i\left(Q_i^g\right)$ denote the cost functions associated with the active and reactive power of the generator i, respectively.

$\mathcal{E}$ represents the set of all transmission lines. θ_{ij} is the stage angle of the transmission line (i, j), where $\theta_{ij} = \theta_i - \theta_j$. G_{ij} and B_{ij} denote the conductance and susceptibility of the transmission line (i, j). P_i^g (Q_i^g) and P_i^d (Q_i^d) represent the generation and load values of active (reactive) power on the bus i. Equations (6) and (7) represent the power balance constraints, reflecting Kirchhoff's current law. Equations (8)-(11) specify the operational limits for generator active power, reactive power, bus voltage, and stage angle differences, ensuring the system operates within a safe and stable range.

3.3. Problem formulation

This study aims to develop a power flow solving framework based on the RC paradigm, integrating physical functional information of the power grid to enrich the priors. The problem can be formally defined as follows:

$$\mathbf{Y} = \mathcal{F}(\mathbf{X}, \mathcal{P}), \tag{12}$$

where $\mathcal{F}$ is the power flow solution function to be designed, $\mathbf{X} \in \mathbb{R}^{N \times 2N_b}$ is the input matrix consisting of the known attribute values of all buses in the power grid, $\mathcal{P}$ represents the additional physical information of the system, and $\mathbf{Y} \in \mathbb{R}^{N \times 2N_b}$ is the output matrix composed of the unknown attribute values. N represents the number of samples and N_b is the number of buses.

More specifically, each row of the input matrix $\mathbf{X}$ corresponds to a system state and can be expressed as:

$$\mathbf{x}_i = [x_{i,1}, x_{i,2}, \ldots, x_{i,2N_b}], \tag{13}$$

where $x_{i,2j-1}$ and $x_{i,2j}$ can represent the two known attribute values of the j-th bus in the i-th sample. For PQ buses, these values are P and Q; for PV buses, they are P and V; and for the slack bus, they are V and θ.

The structure of the output matrix $\mathbf{Y}$ follows a similar structure but includes the unknown values for all buses:

$$\mathbf{y}_i = [y_{i,1}, y_{i,2}, \ldots, y_{i,2N_b}], \tag{14}$$

where $y_{i,2j-1}$ and $y_{i,2j}$ can represent the two unknown attribute values of the j-th bus in the i-th sample. For PQ buses, these values are $\hat{V}$ and $\hat{\theta}$; for PV buses, they are $\hat{Q}$ and $\hat{\theta}$; and for slack bus, they are $\hat{P}$ and $\hat{Q}$.

4. PROPOSED FRAMEWORK

While data-driven methods show promise for power flow calculations, they often struggle to balance computational efficiency with physical consistency, especially under data-scarce conditions. To bridge these gaps, this paper proposes the SMsRC framework, which customizes the RC paradigm by deeply integrating it with power grid physics. Distinct from generic data-driven models, SMsRC introduces three problem-oriented innovations: (1) a Functional Matrix replaces random initialization to explicitly encode the heterogeneous functional roles of grid buses; (2) a Spatial Multi-scale mechanism is constructed to capture both local and global topological dependencies essential for power flow distribution; and (3) Physical Constraints are enforced in the readout layer to ensure solution feasibility while retaining RC's rapid training advantages, avoiding the instability of complex penalty-based loss functions.

The framework aims to learn the solution function $\mathcal{F}$ in Eq. (12) by utilizing additional system information $\mathcal{P} = \{\mathbf{P}_y, \mathbf{P}_t, \mathbf{p}_b, \mathbf{p}_v, \mathbf{p}_x\}$, comprising the admittance matrix $\mathbf{P}_y$, the topological adjacency matrix $\mathbf{P}_t$, the bus-type

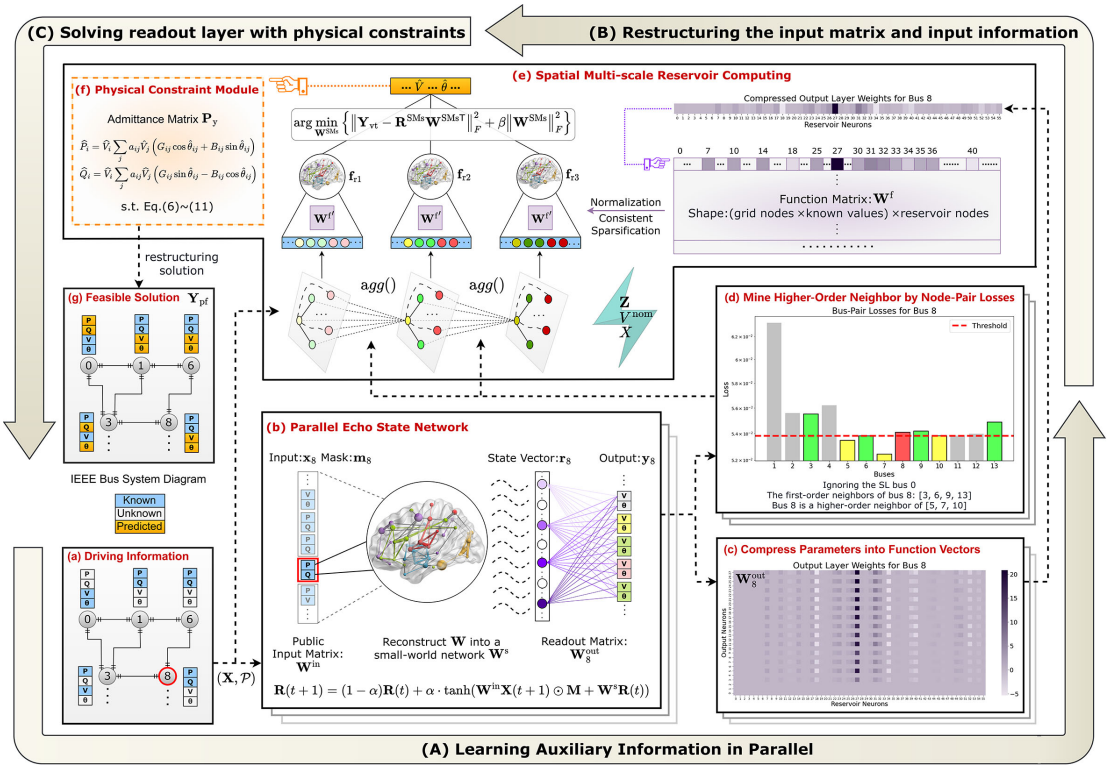

Figure 1. Schematic diagram of the power flow solving framework SMsRC. (a) Driving information and IEEE14 bus system configuration with known/unknown variables. (b) Parallel Echo State Network for initial state learning. (c) Extraction of functional vectors via parameter compression. (d) Identification of higher-order neighbors via node-pair prediction losses. (e) Architecture of the Spatial Multi-scale Reservoir Computing. (f) Physical constraint module for readout layer solving. (g) Final feasible power flow solution.

vector $\mathbf{p}_b$, the nominal voltage vector $\mathbf{p}_v$ and the equivalent reactance vector $\mathbf{p}_x$. Furthermore, $\mathbf{Y}$ is subdivided into intermediate variables $\mathbf{Y}_{vt}$ and the final feasible power flow solution $\mathbf{Y}_{pf}$, where $\mathbf{Y}_{pf}$ depends on $\mathbf{Y}_{vt}$. It is formulated as:

$$\mathbf{Y}_{pf} = \mathcal{F}_{SMsRC}\left(\mathbf{X}, \mathcal{P}, \mathbf{W}^{SMs}\right), \tag{15}$$

where $\mathbf{W}^{SMs}$ denotes the final parameters to be trained in the framework and $\mathcal{F}_{SMsRC}$ represents the solution function of presented SMsRC framework.

The schematic diagram of presented SMsRC framework is presented in Figure 1. To better illustrate, the IEEE14 bus system is considered, as shown in Figure 1(a). A set of driving data, consisting of the known variable values of each bus, together with a set of physical information $\mathcal{P}$, is available. The rectangular box next to each bus displays four variables: P_i, Q_i, V_i, θ_i, where a gray background indicates unknown values, and a blue background denotes known values. By applying parallel learning to all buses as shown in Figure 1(b), two sets of auxiliary information are derived, respectively, as illustrated in Figure 1(c) and (d). Through compression of the weight parameter matrix in Figure 1(c), the functional vector for each bus is obtained, and ultimately the functional vectors of all buses form the functional matrix. Through the Bus-Pair loss (BPLoss) in Figure 1(d), higher-order neighbor information of the buses is extracted, which, combined with physical mechanisms, establishes spatial multi-scale information. In Figure 1(e), the reservoir model, now equipped with spatial multi-scale information and the functional matrix, performs linear regression again. Coupled with the physical constraint module in

Figure 1(f) to reconstruct the readout layer, the feasible solution is obtained in Figure 1(g), where the orange background indicates the final predicted values. In sum, this framework can be divided into three computational stages: (A) Parallel learning auxiliary information; (B) Reconstructing input matrix and input information, and (C) Multi-scale RC with constrained readout layer, which are described as follows.

4.1. Parallel learning auxiliary information

This stage focuses on learning two types of essential auxiliary information for the model: functional feature vectors and higher-order neighbors. The process consists of three steps. First, a parallel ESN architecture is used to generate bus-specific prediction outputs. Second, the resulting parameters are compressed into functional vectors that characterize the unique functional role of each bus. Finally, prediction losses between bus pairs are analyzed to identify higher-order neighbors-buses that exert significant influence despite not being directly connected.

4.1.1. Generating bus-specific prediction outputs via ESNs

First, the conventional ESNs are employed, where each of the N_b power grid buses corresponds to an independent reservoir (see Figure 1(b)). The weighted adjacency matrix $\mathbf{W}$ of the reservoir is then reconstructed as a Watts-Strogatz network[41] $\mathbf{W}^{\mathrm{s}}$, based on the original initialization. All reservoirs share a common input matrix $\mathbf{W}^{\mathrm{in}}$ and $\mathbf{W}^{\mathrm{s}}$, resulting in a total of N_b reservoirs $\mathcal{R}_{\mathrm{pl}} = \{\mathbf{r}_0, \ldots, \mathbf{r}_{N_b-1}\}$. And a mask matrix $\mathbf{M} = [\mathbf{m}_0 : \ldots : \mathbf{m}_{N_b-1}]$ is introduced to filter the original input, ensuring that each reservoir only receives information relevant to its corresponding bus. Then $\mathcal{R}_{\mathrm{pl}}$ undergoes parallel training. This approach leverages local information from a single bus to attempt to predict the global state of all buses. More precisely, the iterative update of the reservoir state $\mathbf{r}_i$ for bus i is given by:

$$\mathbf{r}_i(t+1) = \begin{cases} (1-\alpha)\mathbf{r}_i(t) & t = 1; \\ \quad + \alpha \cdot \tanh\left(\mathbf{W}^{\mathrm{in}}(\mathbf{x} \odot \mathbf{m}_i) + \mathbf{W}^{\mathrm{s}}\mathbf{r}_i(t)\right), & \\ (1-\alpha)\mathbf{r}_i(t) + \alpha \cdot \tanh(\mathbf{W}\mathbf{r}_i(t)), & t > 1. \end{cases} \tag{16}$$

The purpose here is to observe the global state from the perspective of a single local bus with a certain bias.

A set of readout layer weight matrices $\mathcal{W}_{\mathrm{out}} = \{\mathbf{W}_0^{\mathrm{out}}, \ldots, \mathbf{W}_{N_b-1}^{\mathrm{out}}\}$ can be obtained. $\mathbf{W}_i^{\mathrm{out}} \in \mathbb{R}^{N_y \times N_r}$ corresponding to each bus's reservoir exhibits a sparse and inconsistent structure, demonstrating functional localization. As illustrated in Figure 2, the readout layer weights corresponding to buses 1, 2, 3, 8, 9, and 12 are displayed. One can observe that, while all reservoirs in the parallel architecture remain consistent, sharing $\mathbf{W}^{\mathrm{in}}$ and $\mathbf{W}^{\mathrm{s}}$, different buses activate distinct functional partitions within the reservoirs.

4.1.2. Constructing functional feature of each bus via compression operation

Based on above characteristics, $\mathbf{W}_i^{\mathrm{out}}$ is further compressed into a functional feature vector $\mathbf{w}_i^{\mathrm{f}} \in \mathbb{R}^{1 \times N_r}$, defined as the functional feature of the role the bus i plays in the global system, as demonstrated in Figure 1(c). The compression operation is performed to maintain dimensional consistency when subsequently concatenating and reconstructing the multi-scale reservoir input matrix that facilitates a deeper understanding of the role of each bus within the system.

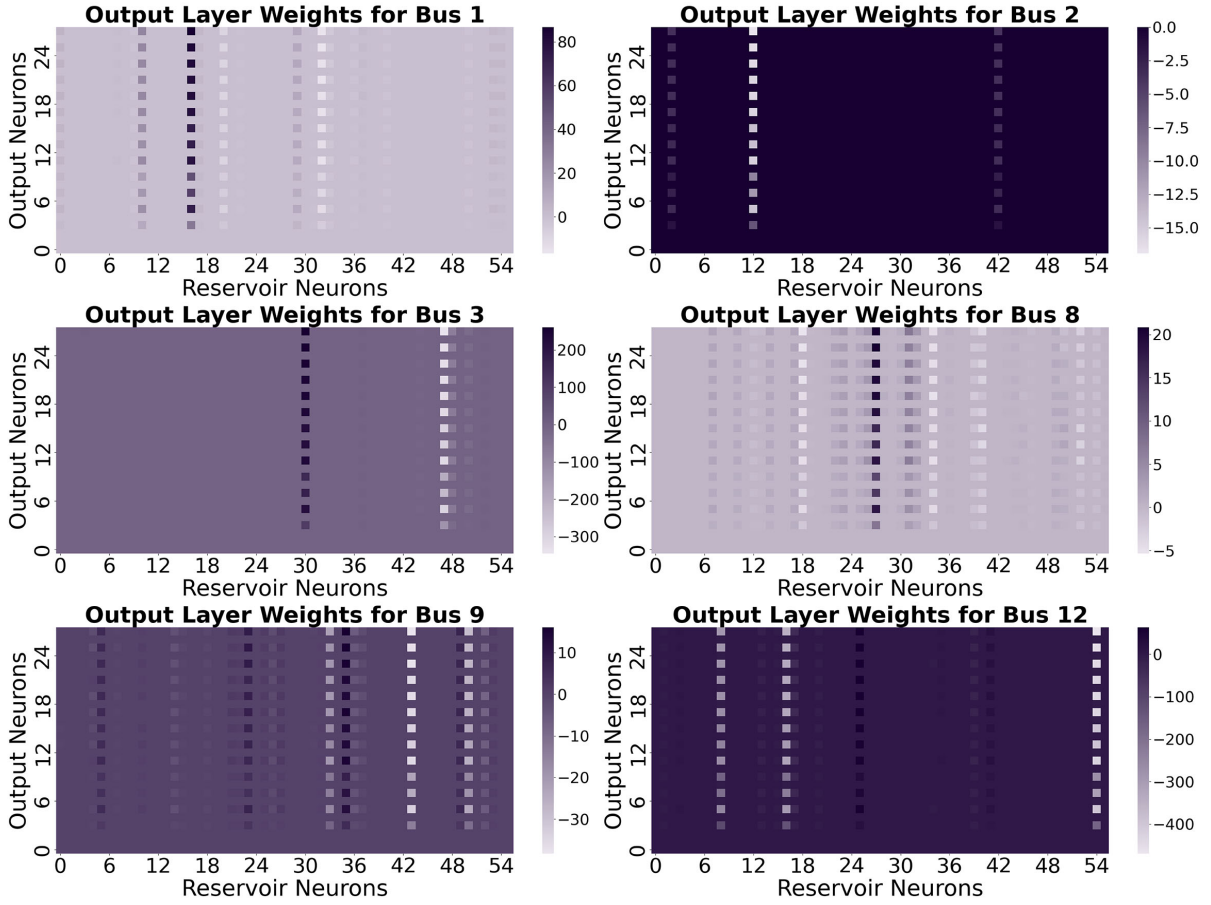

Figure 2. Schematic diagram of functional localization. Visualization of the readout layer weights of the parallel reservoirs corresponding to buses 1, 2, 3, 8, 9, and 12 in the IEEE14 bus system. For this test case, the output dimension is 28, and the number of nodes in each reservoir is 56.

4.1.3. Identifying higher-order neighbors via prediction loss

To uncover deep relationships between different buses, that is, to determine the potential higher-order neighbor information for each bus, the BPLoss metric is introduced to evaluate the loss of each bus relative to others. Define $BPLoss_{i,j} \in \mathbb{R}^{N_b \times N_b}$ as the loss corresponding to bus j within the prediction of the global state, based on the information from local bus i:

$$BPLoss_{i,j} = \frac{100\%}{2} \sum_{k=1}^{2} \left| \frac{\mathbf{y}_{j,k} - \left(\mathbf{W}_i^{\text{out}} \mathbf{r}_i(T)\right)_k}{\mathbf{y}_{j,k}} \right|, \tag{17}$$

where $\sum_{k=1}^{2}$ indicates that the number of unknown attributes for each bus is 2.

Based on the $BPLoss_{i,j}$, the higher-order neighbor set is determined as follows. First, define the threshold for each bus as $TH_i = \min_{j \in \mathcal{N}_i^1 \cup \{i\}} (BPLoss_{i,j})$, where $\mathcal{N}_i^1$ is the topological first-order neighbor set of the bus i. TH_i is the minimum value in the BPLoss of bus i to itself and its first-order neighbors. Then, the higher-order neighbor set is defined as $\mathcal{N}_i^h = \left\{ j \mid BPLoss_{j,i} < TH_j, j \notin \mathcal{N}_i{}^1, i \neq j \right\}$. As shown in Figure 1(d), the $BPLoss_{8,j}$ of bus 8 in the IEEE14 system with respect to other buses is illustrated. $BPLoss_{8,8}$ is marked in red, and the BPLoss of its first-order neighbors is marked in green. The minimum value among the first-order neighbors $\{3, 6, 9, 13\}$ and bus 8 itself, i.e., $\min_{j \in \{3,6,8,9,13\}} \left(BPLoss_{8,j}\right)$, is defined as the threshold TH_8, represented by a red dashed line. Finally, buses marked in yellow $\{5, 7, 10\}$ with $BPLoss_{8,j}$ are below TH_8, and bus 8 is identified as a higher-order neighbor of buses $\{5, 7, 10\}$.

4.2. Reconstructing input matrix and input information

This stage utilizes the two types of auxiliary information from the previous stage to construct two key components: the functional matrix $\mathbf{W}^{\mathrm{f}}$ and the spatial multi-scale information X^{SMs}. First, the functional matrix is assembled to serve as a functionally-aware input mapping for the subsequent reservoirs. Second, physics-informed equivalent transformations are used to generate X^{SMs}, ensuring rational feature aggregation across bus types and enriching the model with prior knowledge.

4.2.1. Constructing the functional matrix

The functional feature vectors $\mathbf{w}_i^{\mathrm{f}}$ of all buses are concatenated into an initial functional matrix $\mathbf{W}^{\mathrm{f}} = [\mathbf{w}_1^{\mathrm{f}}, \mathbf{w}_1^{\mathrm{f}}, \ldots, \mathbf{w}_{N_b}^{\mathrm{f}}, \mathbf{w}_{N_b}^{\mathrm{f}}]^\top \in \mathbb{R}^{2N_b \times N_r}$. The compression operation in the first stage has ensured that the dimensionality of $\mathbf{W}^{\mathrm{f}}$ is the same as that of $\mathbf{W}^{\mathrm{in}}$. Then, through normalization and threshold truncation operations, $\mathbf{W}^{\mathrm{f}}$ is further adjusted to match the distribution range and sparsity of $\mathbf{W}^{\mathrm{in}}$, resulting in the final functional matrix $\mathbf{W}^{\mathrm{f}'}$, which serves as the reconstructed input matrix for the final spatial multi-scale reservoir. These normalization and truncation operations preserve the classic initialization form of the reservoir input matrix. On this basis, rather than completely random sampling, the weights are now derived from the functional matrix $\mathbf{W}^{\mathrm{f}'}$, which guides the information from each bus to different 'functional partitions' [42] within the reservoir, thus guiding the iterative updates of the reservoir in a targeted manner.

4.2.2. Constructing the spatial multi-scale information

Bus information is passed and aggregated based on the neighbor information of buses. However, since the types and attribute values of buses and their neighbors may differ, direct aggregation and summation could lead to inaccuracies or distortions in the information, potentially misleading the model. To address this, the equivalent conversion value based on physical mechanisms is incorporated to ensure physical consistency and validity during the passing process. First, an influence weight w_{ij} is calculated using the impedance matrix $\mathbf{Z}$ of the power grid, namely:

$$w_{ij} = \frac{s}{|\mathbf{Z}_{ij}|} / \sum_{k \neq i} \frac{1}{|\mathbf{Z}_{ik}|}, \tag{18}$$

where $\mathbf{Z}_{ij}$ represents the element in the impedance matrix from bus i to bus j. The parameter s controls the resolution of the generated spatial multi-scale information, which is set to 0.9 empirically. Equation (18) addresses that a smaller impedance implies a stronger influence.

In addition to impedance-based weights, equivalent values are also calculated by simplified power equations using the nominal voltage V^{nom} and the reactance X. For directly connected buses, the reactance values from the branch data are utilized. For non-directly connected buses, the imaginary part of the impedance matrix is utilized. Then, the corresponding information aggregation methods are applied for different types of buses.

Specifically, the P feature of PV and PQ buses, the Q feature of PQ buses, and the V feature of PV buses are respectively aggregated as:

$$P^{(l+1)} = P^{(l)} + \sum_{i \in \mathcal{N}_{PQ}} \mathbf{w}_i \cdot P_i + \sum_{j \in \mathcal{N}_{PV}} \mathbf{w}_j \cdot P_j, \tag{19}$$

$$Q^{(l+1)} = Q^{(l)} + \sum_{i \in \mathcal{N}_{PQ}} \mathbf{w}_i \cdot Q_i + \sum_{j \in \mathcal{N}_{PV}} \mathbf{w}_j \cdot Q_j^{\mathrm{eq}}, \tag{20}$$

$$V^{(l+1)} = V^{(l)} + \sum_{i \in \mathcal{N}_{PV}} \mathbf{w}_i \cdot \left(V_i - V^{(l)}\right) + \sum_{j \in \mathcal{N}_{PQ}} \mathbf{w}_j \cdot V_j^{\mathrm{eq}}, \tag{21}$$

where $Q_j^{\mathrm{eq}} = \frac{V_j^2 - \left(V_j^{\mathrm{nom}}\right)^2}{X_{ij}}$ and $V_j^{\mathrm{eq}} = V_j^{\mathrm{nom}} + \frac{X_{ij} \cdot Q_j}{V_j^{\mathrm{nom}}}$. $\mathcal{N}_{PQ}$ and $\mathcal{N}_{PV}$ denote the set of neighbors (both first-order and higher-order neighbors) of the PQ and PV buses, respectively, and $\mathbf{w}_i$ and $\mathbf{w}_j$ are the corresponding influence weights. $\mathbf{X}$ serves as the original values, and the superscript "eq" indicates equivalent values.

There is only one slack bus in a grid, with unique attribute values that serve as a reference for other buses, so no specific aggregation method is applied to it. Existing studies show that graph message passing often suffers from over-smoothing beyond 2–3 layers[43]. Considering this and the moderate scale of the power grids in this work, this work set the number of aggregation rounds to 2 to balance information utilization and over-smoothing. The spatial multi-scale input set $\mathcal{X}^{\mathrm{SMs}} = \left\{\mathbf{X}, \mathbf{X}^{(1)}, \mathbf{X}^{(2)}\right\}$ is generated through an iterative aggregation process. Specifically, $\mathbf{X}^{(1)}$ is obtained by applying the aggregation rules defined in Eqs. (19)–(21) to the original input $\mathbf{X}$; subsequently,$\mathbf{X}^{(2)}$ is obtained by applying the same aggregation rules to $\mathbf{X}^{(1)}$. This iterative process is analogous to the message-passing mechanism in GNNs, where each aggregation step integrates neighbor information into a higher-order representation.

4.3. Multi-scale RC with physically constrained readout layer

In the third stage, the spatial multi-scale RC (SMsRC) is constructed based on the functional matrix and spatial multi-scale information, as shown in Figure 1(e). To ensure the output solution conforms to actual power grid operation rules without needing an additional optimizer, a physical constraint module is integrated with the readout layer of the SMsRC. The previously improved RC, the efficient training of the RC readout layer, and the physical constraint module together enable the SMsRC framework to both ensure the feasibility of the output and maintain efficiency and precision.

First, the data of each scale in $\mathcal{X}^{\mathrm{SMs}}$ are respectively mapped to the corresponding reservoirs using the same functional matrix $\mathbf{W}^{\mathrm{f}'}$, thus forming three reservoirs denoted as $\mathcal{R}^{\mathrm{SMs}} = \{\mathbf{f}_{\mathrm{r}1}, \mathbf{f}_{\mathrm{r}2}, \mathbf{f}_{\mathrm{r}3}\}$, as illustrated in Figure 1(e). Then, these three reservoirs are connected to a single readout layer for an overall linear regression, which is not only more efficient but also compliant with the computational paradigm of the RC. At this time, the state matrix $\mathbf{R}$ in Eq. (3) is replaced by the more information-rich $\mathbf{R}^{\mathrm{SMs}} = \left[\mathbf{r}_1^{\mathrm{SMs}}(T), \ldots, \mathbf{r}_N^{\mathrm{SMs}}(T)\right]^\top$, with

$$\begin{aligned} \mathbf{r}_n{}^{\mathrm{SMs}}(T) = \Big[& \mathbf{f}_{\mathrm{r}1}\left(\mathbf{W}^{\mathrm{s}}, \mathbf{W}^{\mathrm{f}'}, T, \mathbf{X}_n\right), \\ & \mathbf{f}_{\mathrm{r}2}\left(\mathbf{W}^{\mathrm{s}}, \mathbf{W}^{\mathrm{f}'}, T, \mathbf{X}_n^{(1)}\right), \mathbf{f}_{\mathrm{r}3}\left(\mathbf{W}^{\mathrm{s}}, \mathbf{W}^{\mathrm{f}'}, T, \mathbf{X}_n^{(2)}\right)\Big]^\top. \end{aligned} \tag{22}$$

Now, the spatial multi-scale readout layer weights $\mathbf{W}^{\mathrm{SMs}}$ can be solved by using ridge regression, i.e.,

$$J\left(\mathbf{W}^{\mathrm{SMs}}\right) = \left\|\mathbf{Y}_{\mathrm{vt}} - \mathbf{R}^{\mathrm{SMs}}\mathbf{W}^{\mathrm{SMs}}\right\|_F^2 + \beta\left\|\mathbf{W}^{\mathrm{SMs}}\right\|_F^2. \tag{23}$$

It should be noted that the values obtained are not the final results, but the intermediate variable $\mathbf{Y}_{\mathrm{vt}}$, which represents the values of $\hat{v}$ and $\hat{\theta}$ for all buses. To ensure the feasibility of the solutions and their compliance

with the power grid, additional physical constraints are applied at the readout layer. Specifically, based on the admittance matrix $\mathbf{P}_y$, the variables are reconstructed using the following power flow equations[40]:

$$\hat{P}_i = \hat{V}_i \sum_j a_{ij} \hat{V}_j \left(G_{ij} \cos \hat{\theta}_{ij} + B_{ij} \sin \hat{\theta}_{ij} \right), \tag{24}$$

$$\hat{Q}_i = \hat{V}_i \sum_j a_{ij} \hat{V}_j \left(G_{ij} \sin \hat{\theta}_{ij} - B_{ij} \cos \hat{\theta}_{ij} \right). \tag{25}$$

where G is the real part of the admittance matrix, B is the imaginary part, and this process also adheres to the constraints in Eqs. (6)-(11). Meanwhile, the physical constraint module maintains a low coupling with the overall framework. Finally, the unknown values are obtained for all buses, forming the feasible power flow solution $\mathbf{Y}_{\text{pf}}$.

To further assist the explanation and improve readability, Figure 3 provides a comprehensive flowchart that summarizes the key functional modules and their associated equations across Sections 4.1–4.3. This visual overview clarifies how each stage transforms input data through specific mathematical operations to produce the final feasible power flow solution.

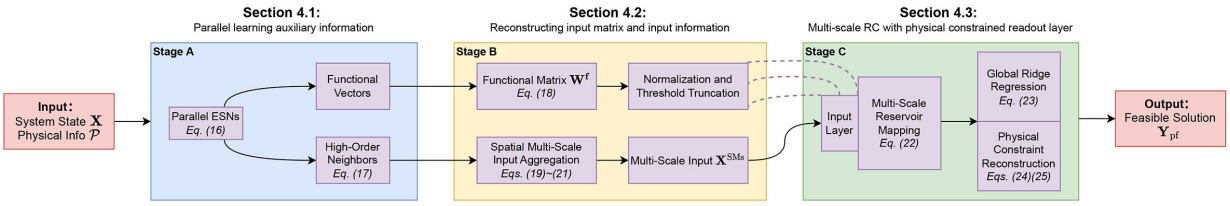

Figure 3. Flowchart summarizing the key components and equations in Sections 4.1–4.3. Section 4.1 (Stage A): Parallel learning extracts functional vectors via reservoir state evolution (Eq. 16) and identifies higher-order neighbors via Bus-Pair loss (Eq. 17). Section 4.2 (Stage B): Constructs the functional matrix (Eq. 18) and generates spatial multi-scale input via physics-informed aggregation (Eqs. 19–21). Section 4.3 (Stage C): Trains multi-scale reservoir (Eq. 22) with ridge regression (Eq. 23) and applies physical power flow constraints (Eqs. 24 and 25) to ensure feasible solutions.

4.4. Algorithm pseudocode

The entire SMsRC can be summarized in Algorithm 1. The algorithm takes input sample data and physical information and outputs the corresponding power flow solution. In the first stage, by initializing the global input matrix $\mathbf{W}^{\text{in}}$ and the reservoir adjacency matrix $\mathbf{W}^{\text{s}}$, the reservoir is constructed for each bus in the system and executed in parallel, and then the readout layer matrix and higher-order neighbors of each bus are identified. In the second stage, the input matrix is reconstructed using the functional matrix, and based on the number of known attribute values k for each bus, the spatial multi-scale input information x^{SMs} is constructed according to Eqs. (19)-(21). In the third stage, the readout layer weights of the spatial multi-scale reservoir are trained, and the solution is reconstructed under physical constraints to obtain the final output.

5. EXPERIMENTS

5.1. Experimental setup

5.1.1. Systems and data

Since the relatively simple structure of IEEE14 system, it is used in Figures 1 and 2, to illustrate the main process of SMsRC. However, it is not included in the main experiments, as its limited complexity makes it difficult to clearly differentiate the performance of various methods. Therefore, the main results are performed in four standard power grid models widely used in the electric power field, i.e., IEEE39, IEEE57, IEEE118, and IEEE300

Algorithm 1 SMsRC for Power Flow Solving.

Input: $\mathbf{X} \in \mathbb{R}^{N \times 2N_b}$, $\mathcal{P} = \{\mathbf{P}_y, \mathbf{P}_t, \mathbf{p}_b, \mathbf{p}_v, \mathbf{p}_x\}$
Output: $\mathbf{Y}_{pf} \in \mathbb{R}^{N \times 2N_b}$

```
/* Stage 1: Parallel Mining */
Initialize global W^in, W^s
Construct M, R_pl
// i = 1 to N_b Parallel jobs
R_i ← r_i(T) ← Eq. (16)
W_out ← Ridge regression to solve W_i^out
for i = 0 to N_b − 1 do
    for j = 0 to N_b − 1 do
        Eq. (17)
    end for
    N_i^h = {j | BPLoss_{i,j} < TH_j, j ∉ N_i^1, i ≠ j}
end for
/* Stage 2: Reconstruct Information */
W^f ← Concatenate w_i^f ← Compress W_i^out
W^f' ← Normalize and truncate W^f
w_{i,j} ← Eq.(18)
for k = 1 to 2 do
    for i = 0 to N_b − 1 do
        X^SMs ← Eqs. (19)-(21)
    end for
end for
/* Stage 3: Solving Under Physical Constraints */
Construct R^SMs = {f_r1, f_r2, f_r3}
R^SMs ← r_n^SMs(T) ← Eq. (22)
W^SMs ← Eq. (23)
Y_pf ← Eqs. (24) and (25) ← Y_vt ← W^SMs · R^SMs
```

systems[44]. Detailed physical information about the system is obtained using tools such as pypower or pandapower[45], and power flow samples, including intermediate variables $\mathbf{Y}_{vt}$ and feasible power flow solutions $\mathbf{Y}_{pf}$, are generated by randomly varying initial values across different grids.

5.1.2. Environment and parameters

The framework is implemented using PyTorch 2.3 and Python version 3.9.19. All experiments are conducted on a CentOS Linux 7.5 machine equipped with a NVIDIA A100-40G GPU, running CUDA version 11.4. The main hyperparameters of the RC model are empirically configured. Specifically, the reservoir size N_r is set to $4 \times N_x$, the reservoir sparsity is 0.1, and the reservoir spectral radius is 0.9. The iteration steps T are set to 5, the leakage rate α is 0.9, and the regularization parameter β is $1 \times e^{-6}$.

5.1.3. Baseline methods for comparison

Since the presented SMsRC is a data-driven methodology based on RC for power flow approximation, the comparison is made with recent data-driven models and other RC-based approaches. Direct comparisons with numerical or heuristic methods are less relevant in this context, as those serve as direct solvers rather than learned approximators.

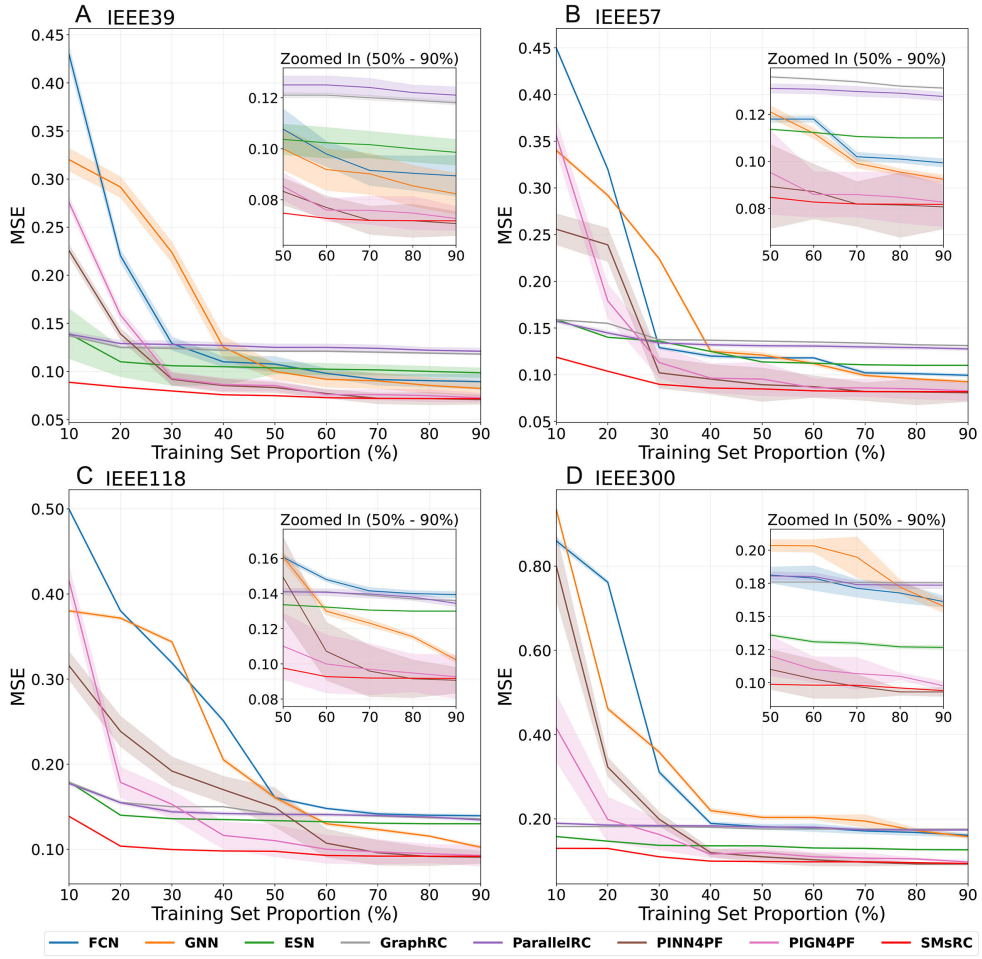

Figure 4. Comparison of MSE performance across four power grids. (A) IEEE39 bus system. (B) IEEE57 bus system. (C) IEEE118 bus system. (D) IEEE300 bus system. Shaded areas indicate the Standard Deviation (STD). Insets show magnified results for training set ratios of 50%–90% for clearer presentation.

- FCN: A method based on fully connected feedforward neural networks for generating power flow solutions [46];
- GNN: A method based on graph neural networks for predicting power flow solution [47];
- ESN: A classical RC approach employing echo state networks to generate power flow solutions [38];
- GraphRC: A RC-based method combined with graph domains, applied to perform power flow calculations [48];
- ParallelRC: A RC-based method with a parallel architecture designed for solving power flow solutions in grids [49];
- PIGN4PF: A physics-informed graph neural network tailored for power flow calculations [50];
- PINN4PF: A physics-informed neural network architecture specifically for power flow calculations [51];

Since methods based on the RC paradigm typically employ ridge regression for solving, to ensure fair evaluation, the outputs of all methods in subsequent experiments are evaluated using the mean square error (MSE) metric.

5.2. Main results

Figure 4 compares the MSE performance of different approaches across four power grids. Several conclusions can be drawn. First, the presented SMsRC framework outperforms other methods, particularly when the training set ratio is below about 50%. Even as the proportion of the training set increases, SMsRC maintains a leading position in most cases, with only a few instances where its performance is matched or slightly surpassed by PINN4PF or PIGN4PF. However, the standard deviation (STD) of SMsRC is smaller than that of PINN4PF and PIGN4PF, indicating better stability. Furthermore, as demonstrated in the next section, SMsRC also excels in computational efficiency compared to these methods.

Second, under data scarcity conditions, RC paradigm shows significant accuracy advantages over non-RC-based methods. This phenomenon can be explained from both architectural and theoretical perspectives. Architecturally, RC only trains the linear readout layer while keeping the reservoir weights fixed, which fundamentally reduces the number of learnable parameters and thus the sample complexity required for reliable generalization[52,53]. Theoretically, the reservoir serves as a high-dimensional nonlinear projection that maps input signals into a rich feature space where different system states become linearly separable[39,54]. This "separation property" enables the simple linear readout to distinguish complex patterns even with limited training samples. Furthermore, the fading memory property (echo state property) of the reservoir ensures that the network state is primarily determined by recent input history rather than requiring extensive data to learn temporal dependencies[37]. Recent studies have further demonstrated that RC can achieve effective predictions even from partial or incomplete observations[55], supporting its robustness in data-scarce scenarios. Consequently, while deep learning methods typically require large datasets for backpropagation-based gradient descent to converge reliably, RC circumvents this bottleneck through its fixed reservoir structure and linear training paradigm.

Third, for RC-based methods, when the amount of data is already sufficient, simply increasing the training samples does little to improve the performance of these models. However, the accuracy of GraphRC and ParallelRC is unsatisfactory, particularly when the training set ratio is higher. This can be attributed to their simple focus on individual nodes and their surroundings, while neglecting higher-order and system-wide information. Although this approach may be sufficient for local-related tasks, power flow calculations require a comprehensive understanding of interactions among bus nodes and the system's overall physical characteristics. Additionally, their incorporation of physical mechanisms is relatively limited.

5.3. Parameter complexity and stable efficiency

First, as summarized in Table 2, this work analyzes the parameter complexity of each method under identical experimental settings, considering factors such as the number of neurons per layer or module and the number of grid buses. The table explicitly presents the parameter count expressions for each method, where n represents the number of buses. It can be observed that, aside from ESN, the basic RC model, SMsRC exhibits superior parameter efficiency compared to the other models.

Then, by fixing the training set ratio at 70%, the comparison of different methods in terms of efficiency with stability and precision is visually presented in Figure 5. It is clear that RC-based methods offer advantages in computational efficiency (i.e., lower running time) and stability (i.e., more consistent MSE values), while physics-informed methods excel in average prediction accuracy. The presented SMsRC framework effectively balances both, particularly standing out as the top performer in terms of both MSE and computational speed on the larger-scale IEEE300 system.

Table 2. Comparison of parameter quantity for different methods. The last column represents the degree of improvement or decrease relative to the SMsRC

Methods	Parameter count	Comparison
FCN	$200n^2 + 30n$	–76%
PINN4PF	$200n^2 + 30n$	–76%
GNN	$296n^2 + 14n$	–83.8%
PIGN4PF	$296n^2 + 14n$	–83.8%
ESN	$16n^2$	+200%
GraphRC	$128n^2$	–62.5%
ParallelRC	$128n^2$	–62.5%
SMsRC	$48n^2 + 128n$	/

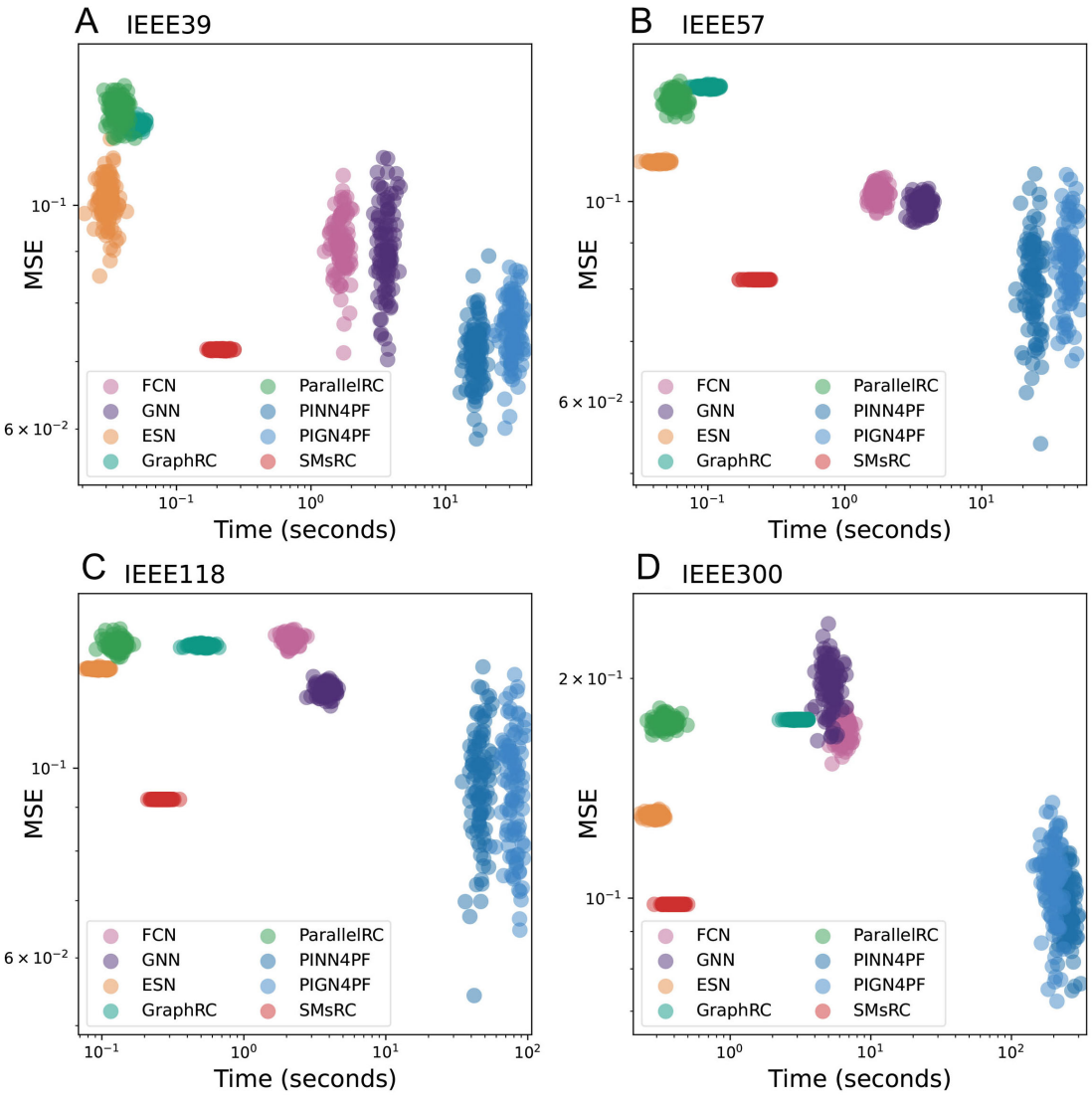

Figure 5. Comparison of efficiency, stability, and accuracy with a fixed training set ratio of 70%. (A) IEEE39 bus system. (B) IEEE57 bus system. (C) IEEE118 bus system. (D) IEEE300 bus system. Each cluster comprises 100 independent experiments, plotting running time (x-axis) against MSE (y-axis) to demonstrate computational speed and solution consistency.

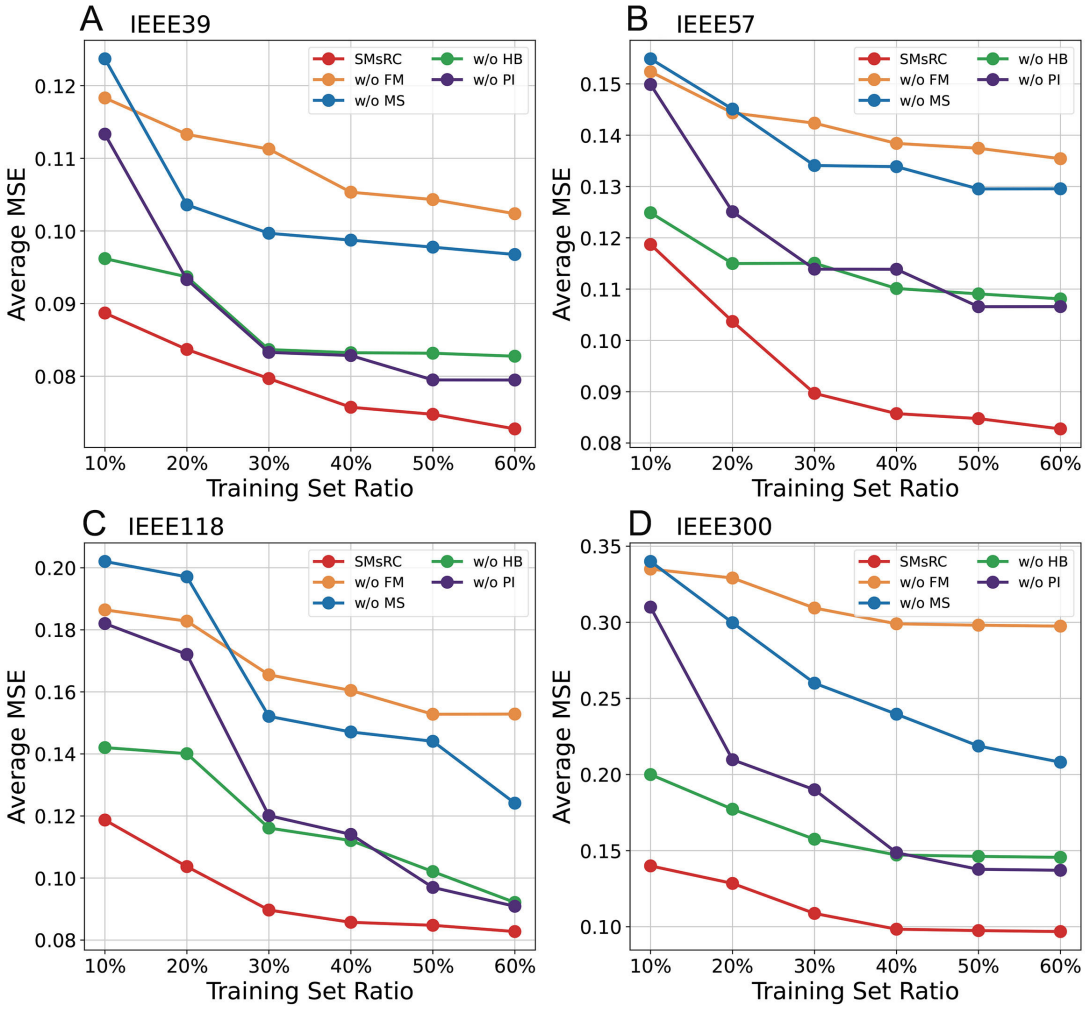

Figure 6. Average MSE of various ablation methods across different datasets. (A) IEEE39 bus system. (B) IEEE57 bus system. (C) IEEE118 bus system. (D) IEEE300 bus system. The ablation settings are defined as: "w/o FM" (without functional matrix), "w/o MS" (without spatial multi-scale mechanism), "w/o PI" (without physical information integration), and "w/o HB" (without higher-order neighbor mining).

5.4. Ablation experiments

The ablation experiments are conducted on the proposed SMsRC framework, as shown in Figure 6. In these experiments, "w/o FM" denotes the ablation of the functional matrix, meaning the random input matrix initialization method is retained. "w/o MS" represents the ablation of the spatial multi-scale component, which effectively reduces the three reservoirs in Figure 1(e) to a single reservoir while maintaining the same total number of reservoir nodes, and it includes "w/o PI" and "w/o HB". "w/o PI" indicates that the framework does not incorporate physical information and relies solely on sample data, with spatial multi-scale information aggregation limited to a simple summation of neighboring attributes. Last, "w/o HB" signifies that the framework no longer uses higher-order neighbor information of buses, considering only topologically first-order neighbors.

In terms of prediction accuracy, the functional matrix and spatial multi-scale are the most critical contributors to the framework, followed by higher-order neighbors and physical information. Additionally, spatial multi-scale and physical information can further enhance stability in data-scarce scenarios. This is evidenced by the steeper curves for the "w/o PI" and "w/o MS" ablation studies, signifying a less stable model transition from data scarcity to normal conditions, and the "w/o MS" setup typically performs worst when the amount of data is minimal.

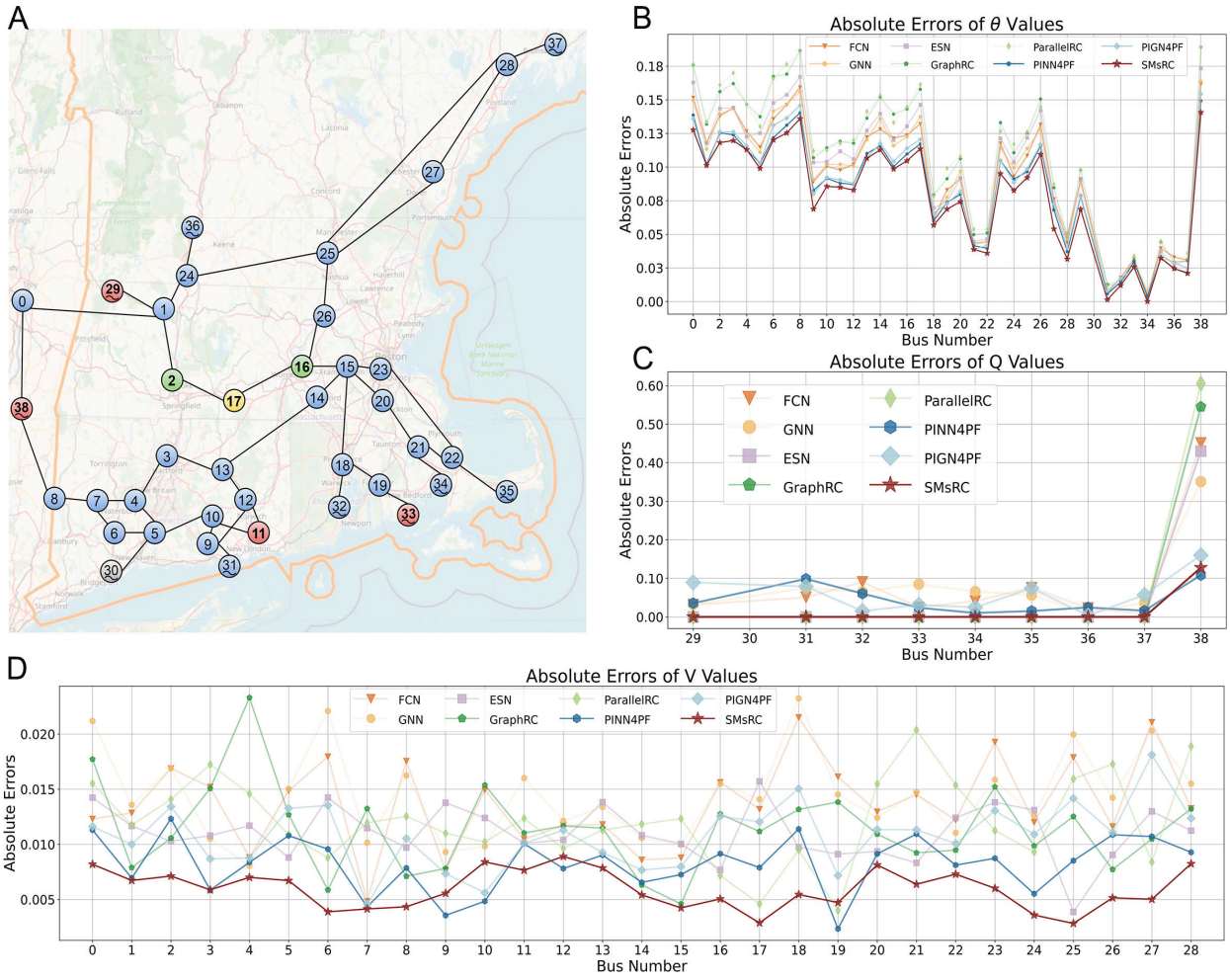

Figure 7. Case analysis of IEEE39 system located in New England. (A) The geographical distribution and connection relationships of 39 buses (Map data ©OpenStreetMap contributors). Green nodes are the direct neighbors of bus 17, and red nodes are the higher-order neighbors of bus 17 identified by SMsRC. (B-D) denote the absolute errors between the model outputs and the true system values for θ, Q and V, respectively.

From a theoretical standpoint, the ablation results validate that each proposed component contributes to enhanced data efficiency in distinct ways. The functional matrix, by encoding deterministic bus-specific roles rather than random weights, provides structured inductive biases that reduce the hypothesis space the model must explore, thereby requiring fewer samples to identify correct mappings[38]. The spatial multi-scale mechanism aggregates information from higher-order neighbors, effectively increasing the information content available per sample by exploiting the inherent correlations in the power grid topology[55]. Finally, the integration of physical information acts as domain-specific regularization, constraining the solution space to physically plausible outputs and preventing overfitting in low-data regimes[56]. These three mechanisms synergistically enhance the framework's sample efficiency, enabling robust performance even when only limited operational data is available.

5.5. Case analysis

Finally, a case study conducted on the 39-bus system in New England is presented in Figure 7. Specifically, Figure 7B-D shows the absolute errors between the model outputs and the true system values: (b) θ values for all buses, (c) Q values for the PV buses, and (d) V values for the load (PQ) buses. All of them again address the great performance of the presented SMsRC approach. Figure 7A also highlights the higher-order neighbors of

bus 17 identified by SMsRC, i.e., buses 11, 29, 33, and 38. Among them, bus 11 is a potentially influential node that may not be intuitively apparent, while buses 29, 33, and 38 are situated in the three generation areas closest to bus 17. Their strong influence on bus 17 aligns well with practical system behavior.

6. CONCLUSIONS

In this work, we leverage the RC paradigm, proposing a SMsRC framework that integrates a functional matrix and physical information. The framework is structured into three main computational stages: parallel learning of auxiliary information, reconstructing the input matrix and input information, and a spatial multi-scale reservoir with a physically constrained readout layer. Together, these stages form a complete and robust power flow solution approach. The main experiments conducted on four standard IEEE bus systems comprehensively validate the effectiveness and advantages of the SMsRC as a power flow solver in terms of computational efficiency, accuracy, generalizability, and robustness. Ablation experiments also validate the critical role of each component.

In future work, we aim to further enhance the presented framework from other perspectives. However, there are still some limitations in this work that merit further investigation. First, regarding the mining of higher-order relationships, the current framework relies on the BPLoss metric. While effective, this metric infers dependencies indirectly based on pairwise prediction errors, and may not fully capture the complex, multi-way interactions inherent in power grid topologies as explicitly as advanced graph-theoretic tools such as hypergraphs or motifs. Second, although the framework demonstrates robustness in data-scarce scenarios, the current study primarily focuses on power flow calculations under steady-state conditions. It has not yet addressed the power flow solvability under scenarios involving dynamic or uncertain factors, such as time-varying load fluctuations, renewable energy intermittency, or extreme events including complex perturbations and cascading failures. Incorporating such factors into the physical constraints would require extending the current static constraint formulation to probabilistic or time-dependent forms, for example, by introducing stochastic programming or robust optimization techniques within the readout layer. Addressing these limitations by integrating hypergraph theory, developing uncertainty-aware physical constraints, and extending the framework to dynamic resilience analysis will be the focus of our future research.

DECLARATIONS

Authors' contributions

Methodology, visualization, and writing-original draft: Zhang, H. F.; Zhang, Y. M.; Ding, X.; Ma, C.
Conceptualization, validation, writing-reviewing, and supervision: Xia, Y.; Tse, C. K.

Availability of data and materials

The raw data supporting the conclusions of this article will be made available by the authors upon request.

Financial support and sponsorship

This work is supported by the National Natural Science Foundation of China (62473001, 62476002), the Hong Kong Research Grants Council under GRF 112015/24, and the City University of Hong Kong (Grant No. 9229105).

Conflicts of interest

All authors declared that there are no conflicts of interest.

Ethical approval and consent to participate

Not applicable.

Consent for publication

Not applicable.

Copyright

© The Author(s) 2026.

REFERENCES

1. Rahman, M.; Islam, M. R.; Hossain, M. A.; Rana, M.; Hossain, M.; Gray, E. M. Resiliency of forecasting methods in different application areas of smart grids: a review and future prospects. *Eng. Appl. Artif. Intell.* **2024**, *135*, 108785. DOI
2. Judge, M. A.; Khan, A.; Manzoor, A.; Khattak, H. A. Overview of smart grid implementation: frameworks, impact, performance and challenges. *J. Energy Storage* **2022**, *49*, 104056. DOI
3. Lopez-Garcia, T. B.; Dominguez-Navarro, J. A. Power flow analysis via typed graph neural networks. *Eng. Appl. Artif. Intell.* **2023**, *117*, 105567. DOI
4. Glover, J. D.; Sarma, M. S.; Overbye, T. Power system analysis and design. 6th ed. Stamford, CT: Cengage Learning; 2017.
5. Milano, F. Continuous newton's method for power flow analysis. *IEEE Trans. Power Syst.* **2009**, *24*, 50-7. DOI
6. Huang, S.; Wang, L.; Xiong, L.; et al. Hierarchical robustness strategy combining model-free prediction and fixed-time control for islanded AC microgrids. *IEEE Trans. Smart Grid* **2025**, *16*, 4380-94. DOI
7. Ding, X.; Wang, H.; Zhang, X.; Ma, C.; Zhang, H. Dual nature of cyber–physical power systems and the mitigation strategies. *Reliab. Eng. Syst. Saf.* **2024**, *244*, 109958. DOI
8. Khaloie, H.; Dolányi, M.; Toubeau, J.; Vallee, F. Review of machine learning techniques for optimal power flow. *Appl. Energy* **2025**, *388*, 125637. DOI
9. Pineda, S.; Perez-ruiz, J.; Morales, J. M. Beyond the neural fog: interpretable learning for AC optimal power flow. *IEEE Trans. Power Syst.* **2025**, *40*, 4912-21. DOI
10. Canyasse, R.; Dalal, G.; Mannor, S. Supervised learning for optimal power flow as a real-time proxy. In 2017 IEEE Power & Energy Society Innovative Smart Grid Technologies Conference (ISGT), Washington, DC, USA, April 23-26, 2017; pp 1-5. DOI
11. Ng, Y.; Misra, S.; Roald, L. A.; Backhaus, S. Statistical learning for DC optimal power flow. In 2018 Power Systems Computation Conference (PSCC), Dublin, Ireland, June 11-15, 2018; pp 1-7. DOI
12. Liu, C.; Li, Y.; Xu, T. A neural network approach to physical information embedding for optimal power flow. *Sustainability* **2024**, *16*, 7498. DOI
13. Grigoras, G.; Cartina, G.; Bobric, E.; Barbulescu, C. Missing data treatment of the load profiles in distribution networks. In 2009 IEEE Bucharest PowerTech (POWERTECH), Bucharest, Romania, June 28-July 2, 2009; pp 1-5. DOI
14. Wringe, C.; Trefzer, M.; Stepney, S. Reservoir computing benchmarks: a tutorial review and critique. *Int. J. Parallel Emergent Distrib. Syst.* **2025**, *40*, 313-51. DOI
15. Li, X.; Zhu, Q.; Zhao, C.; et al. Tipping point detection using reservoir computing. *Research* **2023**, *6*, 0174. DOI
16. Sakemi, Y.; Morino, K.; Leleu, T.; Aihara, K. Model-size reduction for reservoir computing by concatenating internal states through time. *Sci. Rep.* **2020**, *10*, 21794. DOI
17. Gao, L.; Deng, X.; Yang, W. Smart city infrastructure protection: real-time threat detection employing online reservoir computing architecture. *Neural Comput. Applic.* **2021**, *34*, 833-42. DOI
18. Yang, C.; Sun, Y.; Zou, Y.; et al. Optimal power flow in distribution network: a review on problem formulation and optimization methods. *Energies* **2023**, *16*, 5974. DOI
19. Grisales-Norena, L. F.; Montoya, O. D.; Gil-Gonzalez, W. J.; Perea-Moreno, A.; Perea-Moreno, M. A comparative study on power flow methods for direct-current networks considering processing time and numerical convergence errors. *Electronics* **2020**, *9*, 2062. DOI
20. Niu, Z.; Zhang, C.; Li, Q.; Liu, X. Power flow calculation of small impedance branches system based on improved rectangular coordinate newton method. In 2022 5th International Conference on Electronics and Electrical Engineering Technology (EEET), Beijing, China, December 2-4, 2022; pp 110-9. DOI
21. Montoya, O. D. On the existence of the power flow solution in DC grids with CPLs through a graph-based method. *IEEE Trans. Circuits Syst. II.* **2020**, *67*, 1434-8. DOI
22. Tang, Y.; Dvijotham, K.; Low, S. Real-time optimal power flow. *IEEE Trans. Smart Grid* **2017**, *8*, 2963-73. DOI
23. Niu, M.; Wan, C.; Xu, Z. A review on applications of heuristic optimization algorithms for optimal power flow in modern power systems. *J. Mod. Power Syst. Clean Energy* **2014**, *2*, 289-97. DOI
24. Cui, T.; Wang, S.; Qu, Y.; Chen, X. Parameters optimization of electro-hydraulic power steering system based on multi-objective collaborative method. *Complex Eng. Syst.* **2023**, *3*, 2. DOI
25. Bakirtzis, A.; Biskas, P.; Zoumas, C.; Petridis, V. Optimal power flow by enhanced genetic algorithm. *IEEE Trans. Power Syst.* **2002**, *17*, 229-36. DOI
26. Ghasemi, M.; Taghizadeh, M.; Ghavidel, S.; Aghaei, J.; Abbasian, A. Solving optimal reactive power dispatch problem using a novel teaching–learning-based optimization algorithm. *Engineering Applications of Artificial Intelligence* **2015**, *39*, 100-8. DOI

27. Papadimitrakis, M.; Giamarelos, N.; Stogiannos, M.; Zois, E.; Livanos, N.; Alexandridis, A. Metaheuristic search in smart grid: a review with emphasis on planning, scheduling and power flow optimization applications. *Renew. Sustain. Energy Rev.* **2021**, *145*, 11072. DOI
28. Stankovic, S.; Söder, L. Optimal power flow based on genetic algorithms and clustering techniques. In 2018 Power Systems Computation Conference (PSCC), Dublin, Ireland, June 11-15, 2018; pp 1-7. DOI
29. Huang, W.; Pan, X.; Chen, M.; Low, S. H. DeepOPF-V: solving AC-OPF problems efficiently. *IEEE Trans. Power Syst.* **2022**, *37*, 800-3. DOI
30. Bottcher, L.; Wolf, H.; Jung, B.; et al. Solving AC power flow with graph neural networks under realistic constraints. In 2023 IEEE Belgrade PowerTech, Belgrade, Serbia, June 25-29, 2023; pp 1-7. DOI
31. Zhang, H. F.; Lu, X. L.; Ding, X.; Zhang, X. M. Physics-informed line graph neural network for power flow calculation. *Chaos* **2024**, *34*, 113123. DOI
32. Hansen, J. B.; Anfinsen, S. N.; Bianchi, F. M. Power flow balancing with decentralized graph neural networks. *IEEE Trans. Power Syst.* **2023**, *38*, 2423-33. DOI
33. Zhou, Y.; Lee, W.; Diao, R.; Shi, D. Deep reinforcement learning based real-time AC optimal power flow considering uncertainties. *J. Mod. Power Syst. Clean Energy* **2022**, *10*, 1098-109. DOI
34. Nellikkath, R.; Chatzivasileiadis, S. Physics-informed neural networks for AC optimal power flow *Elect. Power Syst. Res.* **2022**, *212*, 108412. DOI
35. Singh, M. K.; Kekatos, V.; Giannakis, G. B. Learning to solve the AC-OPF using sensitivity-informed deep neural networks. *IEEE Trans. Power Syst.* **2022**, *37*, 2833-46. DOI
36. Yan, M.; Huang, C.; Bienstman, P.; Tino, P.; Lin, W.; Sun, J. Emerging opportunities and challenges for the future of reservoir computing. *Nat. Commun.* **2024**, *15*, 2056. DOI
37. Yildiz, I. B.; Jaeger, H.; Kiebel, S. J. Re-visiting the echo state property. *Neural Netw.* **2012**, *35*, 1-9. DOI
38. Lukoševičius, M. A practical guide to applying echo state networks. Berlin Heidelberg: Springer; 2012; pp 659-86. DOI
39. Jaeger, H. The "echo state" approach to analysing and training recurrent neural networks – with an Erratum note. 2001. DOI
40. Wood, A. J.; Wollenberg, B. F.; Sheblé, G. B. Power generation, operation, and control, 3rd ed. Hoboken, NJ: John Wiley & Sons; 2013.
41. Watts, D. J.; Strogatz, S. H. Collective dynamics of 'small-world' networks. *Nature* **1998**, *393*, 440-2. DOI
42. Emelianova, A. A.; Maslennikov, O. V.; Nekorkin, V. I. Higher-order interactions, adaptivity, and phase transitions in a novel reservoir computing model. *Chaos* **2025**, *35*, 103110. DOI
43. Keriven, N. Not too little, not too much: a theoretical analysis of graph (over) smoothing. *Adv. Neural Inf. Process. Syst.* **2022**, *35*, 2268-81. DOI
44. Birchfield, A. B.; Xu, T.; Gegner, K. M.; Shetye, K. S.; Overbye, T. J. Grid structural characteristics as validation criteria for synthetic networks. *IEEE Trans. Power Syst.* **2017**, *32*, 3258-65. DOI
45. Thurner, L.; Scheidler, A.; Schafer, F.; et al. Pandapower - an open-source python tool for convenient modeling, analysis, and optimization of electric power systems. *IEEE Trans. Power Syst.* **2018**, *33*, 6510-21. DOI
46. Yang, Y.; Yang, Z.; Yu, J.; Zhang, B.; Zhang, Y.; Yu, H. Fast calculation of probabilistic power flow: a model-based deep learning approach. *IEEE Trans. Smart Grid* **2020**, *11*, 2235-44. DOI
47. Owerko, D.; Gama, F.; Ribeiro, A. Optimal power flow using graph neural networks. In ICASSP 2020 - 2020 IEEE International Conference on Acoustics, Speech and Signal Processing (ICASSP), Barcelona, Spain, May 4-8, 2020; pp 5930-4. DOI
48. Gallicchio, C.; Micheli, A. Graph echo state networks. In 2010 International Joint Conference on Neural Networks (IJCNN), Barcelona, Spain, July 18-23, 2010; pp 1-8. DOI
49. Srinivasan, K.; Coble, N.; Hamlin, J.; Antonsen, T.; Ott, E.; Girvan, M. Parallel machine learning for forecasting the dynamics of complex networks. *Phys. Rev. Lett.* **2022**, *128*, 164101. DOI
50. Gao, M.; Yu, J.; Yang, Z.; Zhao, J. Physics embedded graph convolution neural network for power flow calculation considering uncertain injections and topology. *IEEE Trans. Neural Netw. Learn. Syst.* **2024**, *35*, 15467-78. DOI
51. Wang, J.; Srikantha, P. Data-driven AC optimal power flow with physics-informed learning and calibrations. In 2024 IEEE International Conference on Communications, Control, and Computing Technologies for Smart Grids (SmartGridComm), Oslo, Norway, September 17-20, 2024; pp 289-94. DOI
52. Lukoševičius, M.; Jaeger, H. Lukoševičius reservoir computing approaches to recurrent neural network training. *Comput. Sci. Rev.* **2009**, *3*, 127-49. DOI
53. Gauthier, D. J.; Bollt, E.; Griffith, A.; Barbosa, W. A. S. Next generation reservoir computing. *Nat. Commun.* **2021**, *12*, 5564. DOI
54. Dambre, J.; Verstraeten, D.; Schrauwen, B.; Massar, S. Information processing capacity of dynamical systems. *Sci. Rep.* **2012**, *2*, 514. DOI
55. Ratas, I.; Pyragas, K. Application of next-generation reservoir computing for predicting chaotic systems from partial observations. *Phys. Rev. E* **2024**, *109*, 064215. DOI
56. Karniadakis, G. E.; Kevrekidis, I. G.; Lu, L.; Perdikaris, P.; Wang, S.; Yang, L. Physics-informed machine learning. *Nat. Rev. Phys.* **2021**, *3*, 422-40. DOI

Disclaimer/Publisher's Note: All statements, opinions, and data contained in this publication are solely those of the individual author(s) and contributor(s) and do not necessarily reflect those of OAE and/or the editor(s). OAE and/or the editor(s) disclaim any responsibility for harm to persons or property resulting from the use of any ideas, methods, instructions, or products mentioned in the content.

© The Author(s) 2026. **Open Access** This article is licensed under a Creative Commons Attribution 4.0 International License (https://creativecommons.org/licenses/by/4.0/), which permits unrestricted use, sharing, adaptation, distribution and repro-duction in any medium or format, for any purpose, even commercially, as long as you give appropriate credit to the original author(s) and the source, provide a link to the Creative Commons license, and indicate if changes were made.